Applying Spatio-Temporal Analytics to Quantify Sub-Sampled Operando (S)TEM Images Mapping Nanoscale Chemical Dynamics

Andrew N. Other,[†,§] Fred T. Secondauthor,[†,‖] I. Ken Groupleader,[*,†,‡,§] Susanne K. Laborator,[*,¶] and Kay T. Finally[†,‡]

†*Department of Chemistry, Unknown University, Unknown Town*

‡*Department of Chemistry, Second University, Nearby Town*

¶*Lead Discovery, BigPharma, Big Town, USA*

§*A shared footnote*

‖*Current address: Some other place, Othertöwn, Germany*

E-mail: i.k.groupleader@unknown.uu; s.k.laborator@bigpharma.co

Phone: +123 (0)123 4445556. Fax: +123 (0)123 4445557

Abstract

One of the main limitations in the use of operando scanning transmission electron microscopes to study dynamic chemical processes is the effect of the electron beam on the kinetics of the reaction being observed. Here we demonstrate that a flexible Gaussian mixture model can be used to extract quantitative information directly from sub-sampled images, i.e. images where not all the pixels in the image are illuminated with the beam. The use of this method is demonstrated for the charge/discharge cycle

of a Li-battery, where the deposition and dissolution of Li at the anode can be accurately quantified for sub-sampling levels down to ≈1%. Performing operando imaging using a small fraction of the pixels means that the observations can significantly reduce the effect of the beam, automatically increase the imaging speed and decrease the total data transfer rate required. Such new software capabilities offer the potential to significantly widen the application of operando hardware approaches to study nanoscale dynamics in materials.

Abbreviations

TBD

Keywords

Operando (S)TEM, sub-sampled images, Gaussian mixture model, Li-batteries

Introduction

Nigel's citations:

[1] ?

[2-4] ?

[5] ?

[11] ?

Although aberration corrected (scanning) transmission electron microscopes (S/TEM) can now routinely obtain spatial resolution on the atomic scale from stable samples, the

high electron beam dose that is typically used severely limits the range of samples that can be studied without significant beam damage [1]. In-situ or Operando TEM, where a chemical reaction is observed in either a gas or liquid stage [2-4], has even more strict tolerances on the doses that can be used to image the sample as the beam can change the kinetics of the reaction [5]. This limitation has led to several recent successful efforts to sub-sample the images during acquisition, i.e. apply electron dose to fewer pixels in the image, and use compressive sensing/in-painting mathematical methods to reconstruct the images after acquisition [6-10].[1–5] This reconstruction is, however, the time consuming step in the process and in many cases the images themselves are not the important part of the result - it is the quantitative information extracted from the images that is used to understand the material or process [11]. Here we demonstrate that a flexible Gaussian mixture model (GMM) can be used to extract quantitative information directly from the sub-sampled images bypassing the necessity to reconstruct the images. The use of this method is demonstrated for the charge/discharge cycle of a Li-battery,[6] where the deposition and dissolution of Li on the anode can be accurately quantified for sub-sampling levels down to below 1%.

In order to quantify the information in the STEM images we can segment the image into a simpler representation of the structures and processes within. Some methods have already used segmentation by combining a superposition of Gaussian peaks on the observed pixel intensities and a maximum likelihood estimator[7,8] to determine unknown structure parameters.[9–15] Such observations often aim to reduce the dose and run in an energy filtered mode, but they indicate that the accuracy of the measurements is not generally controlled by the sampling of the image itself.[16] Approaches used previously to quantify in-situ images have used thresholding techniques[17,18] or physical models[19–21] for example, but these methods often require the highest resolution images possible and in general the models do not generalize to multiple experiments well. Our goal here is to determine a way to routinely analyze sub-sampled images in real-time/near real-time from a video datastream acquired

by the microscope. We accomplish this by using a Gaussian mixture model with simultaneous background correction. The methodology involves three main steps. Firstly a Gaussian mixture regression model (GMRM) is fit to the raw data in order to partition the pixels into distinct clusters while simultaneously accounting for spatial trends in intensity. Secondly, the clusters are partitioned into foreground and background based on the cluster distributions. Finally, a post-hoc spatio-temporal correction is applied to the foreground and background classifications to account for noise. These spatio-temporal clusters of pixels then contain the quantified information desired from the experiment (for full details of this approach see Johnson et al. 2017[22]).

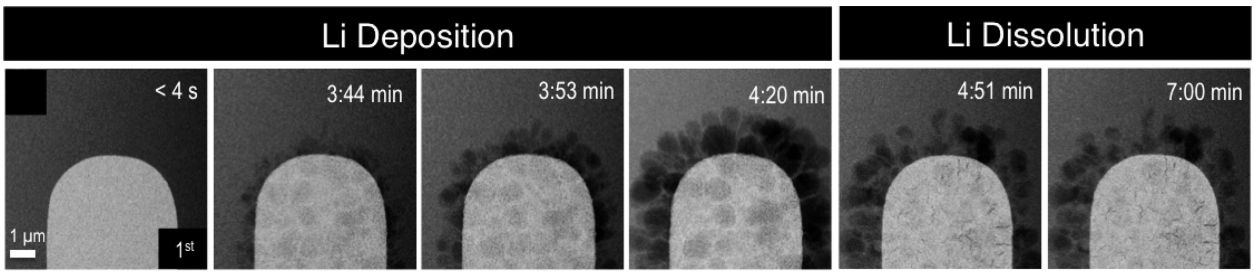

Figure 1: High-angle annular dark field (HAADF) images of Li deposition and dissolution at the interface between the Pt working electrode and the $LiPF_6$/PC electrolyte during a charge/discharge cyles of the operando cell. The formation of the SEI layer (ring of contrast around the electrode), alloy formation due to Li^+ ion insertion, and the presence of "dead Li" detached from the electrode can all be seen in the images at the end of the cycle, thereby demonstrating the degree of irreversibility associate with the process.

The data stream that we will use for this test is a movie (Supplementary Movie SM1) acquired while a Li-battery electrolyte was subjected to a CV scan (Figure 1). During the scan the electrolyte breaks down during the "charging" of the battery and Li is seen to be deposited on the anode. When the voltage is reversed and the battery is "discharging," Li goes back into solution. However, upon completion of the cycle there is still Li remaining on the anode indicating that the process is not 100% Coulombic efficient and Li dendrites will form in the system upon repeated cycling. The key question for the design of an improved battery is to know how much Li is deposited, in what form and how much is stripped during

the reverse cycle. The images shown in Figure 1 are obtained from the STEM[23] operating in mass-thickness contrast mode where each pixel is on a greyscale with values from 0 to 255. A particular peculiarity in this set of images is that the Li is the lightest/least dense component of the system and so this shows up as the brightest part of the image (the contrast is reversed from the Pt anode which is the hemispherical dark feature in the image). Everything not "white" Li or "black" Pt is where the liquid electrolyte is. There are also other features in the image such as a general trend in contrast across the image that may change during the experiment as the microscopist repositions the specimen or changes magnification/focus. In addition, noise is present which means the same pixel may not be consistent from image to image. All of these features complicate the algorithm designed to quantify the contrast.

The first step in analyzing this data stream (Supplementary Movie SM1) is to partition the frame into groups with similar intensity distributions, i.e. the distribution of intensities across the image is assumed to be multi-modal where each mode is associated with a different characteristic. Figure 2 is an example of a frame taken from a fully sampled movie of Li deposition during battery charging (Supplementary Movie SM1). The three modes shown in the distribution of pixel intensities in Figure 2b are associated with the anode (red), the Li-deposits (blue) and the liquid electrolyte (green) in the system. Visually the pixel intensity distribution can be described by a mixture of normal distributions with different means (centers) and variances (widths) - and thus a Gaussian mixture model is fit to the image. Let $\boldsymbol{z} = (z_1, \ldots, z_n)$ represent the vector of n pixel intensities in the frame, and $\boldsymbol{C}$ be an $n \times K$ matrix of indicator variables that identifies which cluster into which each cluster belongs. That is if $k = 3$ then $C_{i,1} = 1$ if pixel i belongs to class 1 while $C_{i,2} = C_{i,3} = 0$. Then the distribution of pixel intensities is described by the likelihood

$$p(\boldsymbol{z}, \boldsymbol{C}|\boldsymbol{\theta}) = \prod_{i=1}^{n} \prod_{k=1}^{K} [p_k N(z_i; \delta_k, \sigma_k)]^{C_{ik}} \tag{1}$$

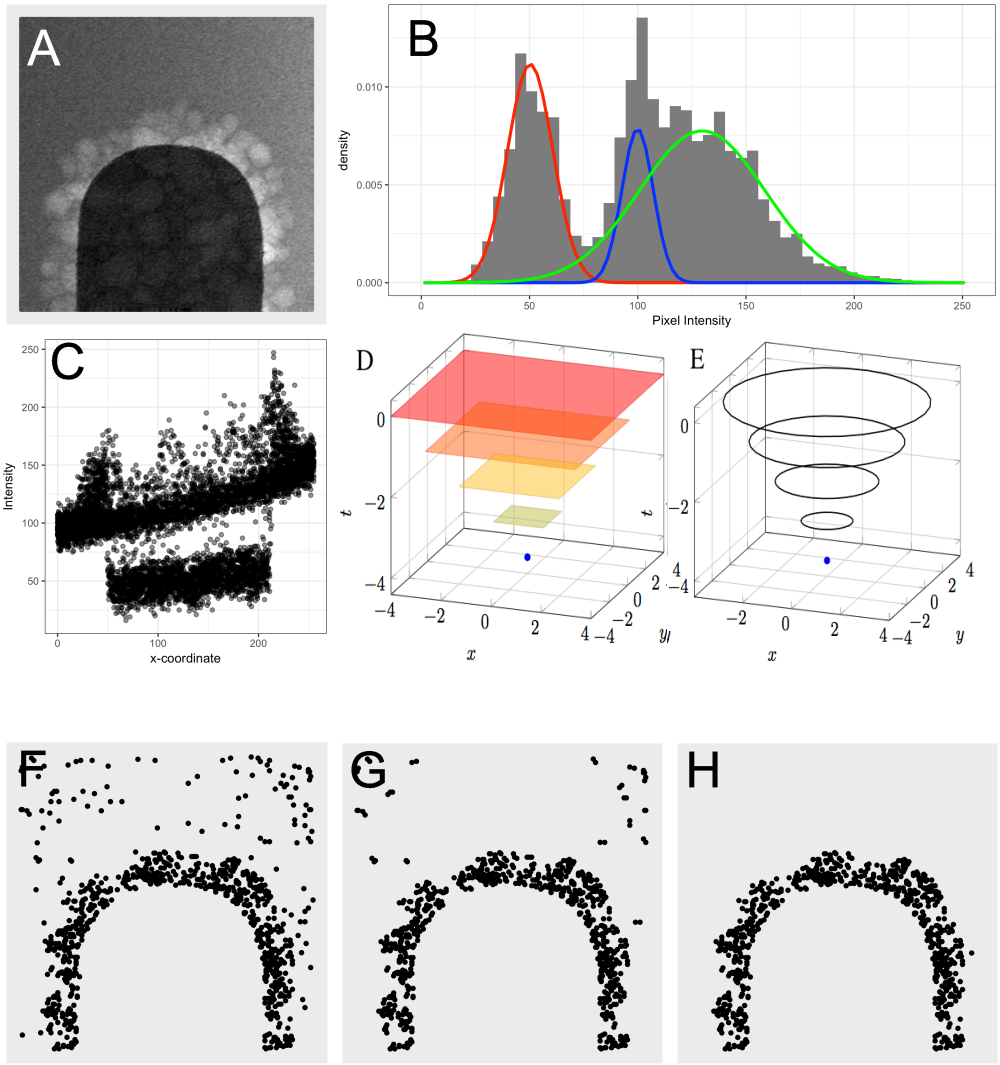

Figure 2: An image from the experiment during the Li deposition phase (a) shows the growth of Li around the anode. The histogram of pixel intensity values illustrates that a mixture of three normal distributions captures the important features of the image (b). The linear increase in pixel intensity from the left to right of the image demonstrates the need for a background correction component (c). The spatio-temporal correction of the pixel classifications can be done with using the three-dimensional L_2 (d) or L_1 (e) distance placed on a regular grid. The effectiveness of the spatio-temporal correction of initial growth/background pixel classifications (f) is affected by the parameters γ and r. Figures (g) and (h) illustrate the effect of the spatio-temporal correction with different parameters, $(r = 5, \gamma = 0.05)$ and $(r = 20, \gamma = 0.2)$, respectively.

where K is the number of mixture components, $\boldsymbol{p} = (p_1, \ldots, p_K)^\top$ is a K-dimensions vector of mixture component weights, $\boldsymbol{\delta} = (\delta_1, \ldots, \delta_K)^\top$ is a K-dim vector of group means, and

$\boldsymbol{\sigma} = (\sigma_1, \ldots, \sigma_K)^\top$ is a K-dim vector of components standard deviations and $\boldsymbol{\theta} = (\boldsymbol{p}, \boldsymbol{\delta}, \boldsymbol{\sigma})$.

Because the cluster labels are missing for each pixel, i.e., $\boldsymbol{C}$ is unobserved, the unknown parameter vector $\boldsymbol{\theta}$ is estimated using the expectation maximization (EM) algorithm.[24] In addition to an estimate for the parameter vector $\boldsymbol{\theta}$, the EM algorithm estimates the probability that each pixel belongs in each of the clusters. Each pixel is initially classified into the group that is estimated to be the most likely.

STEM images often exhibit systematic trends in grayscale that must be accounted for (Figure 2c). This gradient can be due to effects such as charging, thickness variations, carbon contamination etc and must be accounted for with the analytics. Image segmentation methods based on standard Gaussian mixture models or thresholding will not work when trends are present as the background intensities take a functional form rather than a static threshold. We extend the model defined by Equation 1 by adding a regression-based approach to account for systematic trends in background. When accounting for the grayscale gradient, the mean for each distribution, δ_k, plays the role of an intercept in a regression model with inputs, $f_j(x_i, y_i)$ where (x_i, y_i) define the spatial location of pixel i in the image and $f_j(\cdot, \cdot)$ is some function of (x_i, y_i) for $j = 1, \ldots, q$. The the model for pixel intensities in Equation 1 is extended to

$$p(z_i|\boldsymbol{\theta}) = \prod_{i=1}^{n} \prod_{k=1}^{K} \left[p_k N\left(z_i; \sum_{j=1}^{q} \beta_j f_j(x_i, y_i) + \delta_k, \sigma_k \right) \right]^{C_{ik}} \tag{2}$$

where $\boldsymbol{\beta} = (\beta_1, \ldots, \beta_j)^\top$ is a q-dim vector of trend coefficients. Due to the global trend in gray scale values, a modified version of the EM algorithm, called the expectation/conditional maximization algorithm (ECM),[25] is required to estimate the parameters in the likelihood defined by Equation 2. See Johnson et al. (2017)[22] for a full derivation of the algorithm.

The functions used to model the intensity gradient $f_j(x_i, y_i)$ are dependent upon the hypothesized gradient and they must be chosen appropriately. Common choices include a

linear trend in the x direction, $f_j(x_i, y_i) = x_i$, quadratic trend in the x direction, $f_j(x_i, y_i) = x_i^2$ and similarly in the y-direction. If an anode is in the video, e.g. Figure 2a, then the linear and quadratic trends in x will vary depending upon the y value implying the functions $f_j(x_i, y_i) = x_i y_i$ and $f_j(x_i, y_i) = x_i^2 y_i$ should be included in the model. To determine the most appropriate intensity gradient function, model comparison metric such as AIC and BIC can be used to compare models while likelihood ratio test can be used to test nested models (double check this is appropriate for EM algorithm).

The initial classifications returned by the ECM algorithm with and without background correction can often be improved by incorporating spatio-temporal information about each pixel. Ideally the spatio-temporal trends are built into the algorithm itself but that renders it too computationally expensive. Thus we enforce spatio-temporal coherence by implementing a post hoc spatio-temporal correction on already clustered pixels from the GMRM. In short a spatio-temporal neighborhood is defined around each pixel and the proportion of pixels in that neighborhood belonging to each group is computed. If a pixel of interest is classified differently from a given percentage of neighboring pixels, the classification is changed to match the neighbors. Let $(x_i, y_i)_t$ denote the (x, y) coordinate of the ith pixel at time t. Then the neighborhood for the ith pixel is defined by all pixels i' at time $t' < t$ such that

$$d\left[(x_i, y_i)_t, (x_{i'}, y_{i'})_{t'})\right] \leq c \tag{3}$$

for some chosen value c. Specific examples of distance metrics are the L_1 and L_2 distances, which, in the context of Equation 3, are of the form $|x_i - x_{i'}| + |y_i - y_{i'}| + |t - t'| \leq c$ (Figure 2d) and $(x_i - x_{i'})^2 + (y_i - y_{i'})^2 + (t - t')^2 \leq c^2$ (Figures 2e), respectively . Examples of the effect of spatio-temporal correction on the image data stream is shown in Figure 2f, g and h. Once the data stream is classified in this way, any number of quantitative features can be extracted based on pixel contrast.

Because the experiment that produced the movie SM1 was fully sampled, we can test the effect of sub-sampling by randomly sampling the data stream with a proportion of the pixels. An example of this is given in Figure 3, which shows only the pixels classified Li dendrite formation based on the GMRM with $K = 4$ components when only 10% of each frame is sampled. The methodology appeared to classify pixels as Li growth well in the first CV cycle (supplementary movie SM1), though these estimates of growth are likely subject to bias and may be noisy.

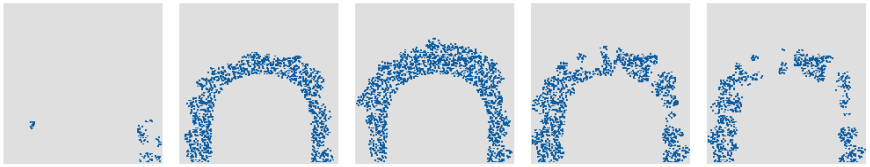

Figure 3: Li classification corresponding to the images from Figure 1 using the linear GMRM on 10% sampled images. The classifications were corrected with $r = 10$ and $\gamma = 0.4$.

To quantify the effect of sampling a fraction of the pixels in the image on estimating the volume of Li growth, the video SM1 was analyzed several times with three different sampling rates: 10, 5 and 1%. To make the results derived from different sampling rates comparable, the number of times the video was analyzed, denoted B, for each sampling rate was chosen such that the each pixel was expected to have been sampled 10 times. For example, for the 1% sampling scheme, each pixel has a 1% chance of being chosen, thus the video was analyzed $B = 1,000$ times so that each pixel is expected to be sampled $1000 \times 0.01 = 10$ times. The number of replicates, B, for each sampling rate is reported in Table 1.

Table 1: Average (Avg.) bias and uncertainty bound width of the GMRM method for the different sampling rates considered. Bias was computed as the difference in the estimated volume using a subset of the pixels and the volume estimated using the full image. The width of the uncertainty bound was taken to be the difference in the 90^{th} and 10^{th} percentiles. Both quantities were averaged over the course of the experiment.

Sampling Rate	Num. Replicates (B)	Avg. Bias (μm^3)	Avg. Width (μm^3)
10%	100	0.094	0.703
5%	200	0.332	1.121
1%	1,000	2.012	6.001

Figure 4(a) illustrates the bias introduced by sub-sampling scheme by plotting the average of the B growth curves for each of the sampling rates along with the estimated growth curve when 100% of the pixels are used, which was treated as the true growth curve. Additionally, the bias for each method averaged over the course of the experiment is reported in Table 1. For each sampling rate, the volume of Li growth was overestimated for vast a majority of the experiment, and the degree of bias decreased when more pixels were sampled. The 1% sampling rate exhibits a significant bias at the beginning and ending of the experiment, but that bias is significantly reduced when the reaction transitions from deposition to dissolution. The growth curves for 5% and 10% sampling show a dramatic reduction in bias and visually appear to agree, but the average bias did drop by 72% when the sampling rate was increased to 10%. In particular, the estimated Li growth using a 10% sampling is less than $1\mu m^3$ away from the true growth on average.

The uncertainty induced by the different random sampling schemes is illustrated in Figures 4 (b), (c) and (d), in which the 10^{th} (red), 50^{th} (solid black) and 90^{th} (red) percentiles of the repeated growth curves at different sampling rates are plotted along with the growth curve estimated using all of the pixels (dashed black). As such, there is an 80% chance that if this experiment were analyzed again at a specified sampling rate, the resultant growth curve would lie between the two red lines in the respective figure. For all sampling rates, the true growth curve is contained within the uncertainty bands throughout the course of

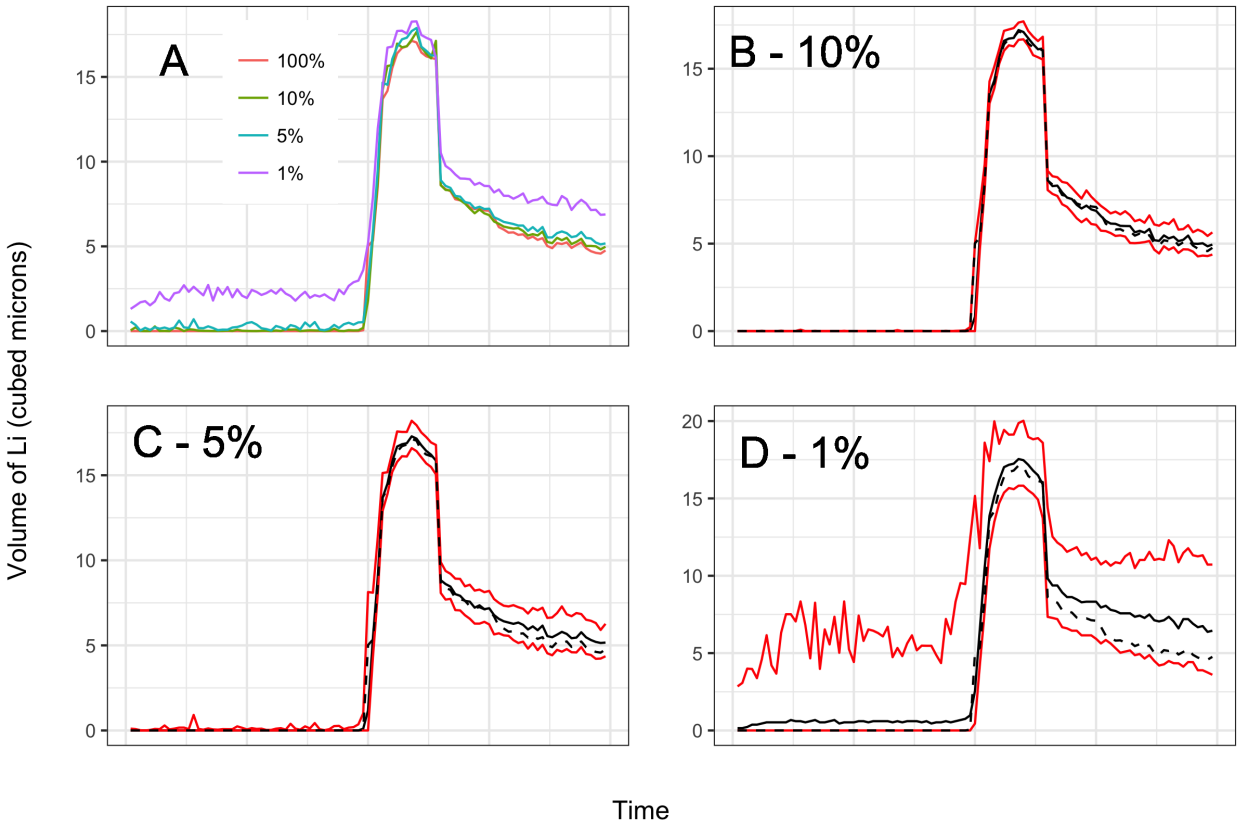

Figure 4: Comparison of the estimated volume of the Li deposited at the Pt electrode-$LiPF_6$/PC electrolyte interface quantified by the GMRM algorithm when the image was fully sampled (100%), and down sampled (10%, 5% and 1%)(a). For the downsampled images, the analysis was repeated multiple times to assess the uncertainty associated with downsampling strategy. The 10^{th} (red), 50^{th} (solid black) and 90^{th} (red) percentiles of the repeated analyses are plotted for the 10% (b), 5% (c) and 1% (d) sampling rates. The dashed line in Figures (b), (c) and (d) represents the growth curve estimated using all of the pixels.

the experiment. The widths of the uncertainty bands for the different sampling rates are reported in Table 1. The uncertainty bounds widen as the sampling rate decreases with a significant decrease in uncertainty when the sampling rate is increased from 1% to 5%.

Conclusion

Acknowledgement

Please use "The authors thank ..." rather than "The authors would like to thank ...".

The author thanks Mats Dahlgren for version one of achemso, and Donald Arseneau for the code taken from cite to move citations after punctuation. Many users have provided feedback on the class, which is reflected in all of the different demonstrations shown in this document.

References

1. Candès, E. J.; Romberg, J.; Tao, T. Robust uncertainty principles: Exact signal reconstruction from highly incomplete frequency information. *IEEE Transactions on information theory* **2006**, *52*, 489–509.

2. Donoho, D. L. Compressed sensing. *IEEE Transactions on information theory* **2006**, *52*, 1289–1306.

3. Stevens, A.; Yang, H.; Carin, L.; Arslan, I.; Browning, N. D. The potential for Bayesian compressive sensing to significantly reduce electron dose in high-resolution STEM images. *Microscopy* **2014**, *63*, 41–51.

4. Stevens, A.; Kovarik, L.; Abellan, P.; Yuan, X.; Carin, L.; Browning, N. D. Applying

compressive sensing to TEM video: a substantial frame rate increase on any camera. *Advanced Structural and Chemical Imaging* **2015**, *1*, 10.

5. Kovarik, L.; Stevens, A.; Liyu, A.; Browning, N. D. Implementing an accurate and rapid sparse sampling approach for low-dose atomic resolution STEM imaging. *Applied Physics Letters* **2016**, *109*, 164102.

6. Mehdi, B. L.; Qian, J.; Nasybulin, E.; Park, C.; Welch, D. A.; Faller, R.; Mehta, H.; Henderson, W. A.; Xu, W.; Wang, C. M. *et al.* Observation and Quantification of Nanoscale Processes in Lithium Batteries by Operando Electrochemical (S)TEM. *Nano Letters* **2015**, *15*, 2168–2173.

7. den Dekker, A. J.; Aert, S. V.; van den Bos, A.; ; Dyck, D. V. Maximum likelihood estimation of structure parameters from high resolution electron microscopy images. Part I: A theoretical framework. *Ultramicroscopy* **2005**, *104*, 83–106.

8. Aert, S. V.; den Dekker, A.; van den Bos, A.; Dyck, D. V.; Chen, J. Maximum likelihood estimation of structure parameters from high resolution electron microscopy images. Part II: A practical example. *Ultramicroscopy* **2005**, *104*, 107–125.

9. Bals, S.; Aert, S. V.; Tendeloo, G. V.; Ávila-Brande, D. Statistical estimation of atomic positions from exit wave reconstruction with a precision in the picometer range. *Physical Review Letters* **2006**, *96*, 096106.

10. Bals, S.; Aert, S. V.; Romero, C.; Lauwaet, K.; Bael, M. J. V.; Schoeters, B.; Partoens, B.; Yücelen, E.; Lievens, P.; Tendeloo, G. V. Atomic scale dynamics of ultrasmall germanium clusters. *Nature Communications* **2012**, *3*, 897.

11. Aert, S. V.; Turner, S.; Delville, R.; Schryvers, D.; Tendeloo, G. V.; Salje, E. K. Direct observation of ferrielectricity at ferroelastic domain boundaries in CaTiO3 by electron microscopy. *Advanced Materials* **2012**, *24*, 523–527.

12. Aert, S. V.; Backer, A. D.; Martinez, G.; Goris, B.; Bals, S.; Tendeloo, G. V.; Rosenauer, A. Procedure to count atoms with trustworthy single-atom sensitivity. *Physical Review B* **2013**, *87*, 064107.

13. Martinez, G.; Rosenauer, A.; Backer, A. D.; Verbeeck, J.; Aert, S. V. Quantitative composition determination at the atomic level using model-based high-angle annular dark field scanning transmission electron microscopy. *Ultramicroscopy* **2014**, *137*, 12–19.

14. Kundu, P.; Turner, S.; Aert, S. V.; Ravishankar, N.; Tendeloo, G. V. Atomic structure of quantum gold nanowires: quantification of the lattice strain. *ACS Nano* **2014**, *8*, 599–606.

15. Backer, A. D.; ; van den Bos, K.; ; den Broek, W. V.; Sijbers, J.; Aert, S. V. StatSTEM: An efficient approach for accurate and precise model-based quantification of atomic resolution electron microscopy images. *Ultramicroscopy* **2016**, *171*, 104–116.

16. Backer, A. D.; Martinez, G.; MacArthur, K.; Jones, L.; Béché, A.; Nellist, P.; Aert, S. V. Dose limited reliability of quantitative annular dark field scanning transmission electron microscopy for nano-particle atom-counting. *Ultramicroscopy* **2015**, *151*, 56–61.

17. Abellan, P.; Woehl, T. J.; Parent, L. R.; Browning, N. D.; Evansc, J. E.; Arslan, I. Factors influencing quantitative liquid(scanning) transmission electron microscopy. *Chem. Comm.* **2014**, *50*, 4873–4880.

18. Wang, Z. A new approach for segmentation and quantification of cells or nanoparticles. *IEEE Transactions on Industrial Informatics* **2016**, *12*, 962–971.

19. Evans, J. E.; Jungjohann, K. L.; Arslan, N. D. B. I. Controlled growth of Nanoparticles from solution with *in situ* liquid transmission electron microscopy. *Nano Letters* **2011**, *11*, 2809–2813.

20. Bridges, C. A.; Sun, X.-G.; Zhao, J.; Paranthaman, M. P.; Dai, S. In Situ Observation of Solid Electrolyte Interphase Formation in Ordered Mesoporous Hard Carbon by Small-Angle Neutron Scattering. *Journal of Physical Chemistry* **2012**, *116*, 77017711.

21. Zeng, Z.; Liang, W.-I.; Liao, H.-G.; Xin, H. L.; Chu, Y.-H.; Zheng, H. Visualization of electrode–electrolyte interfaces in LiPF6/EC/DEC electrolyte for lithium ion batteries via in situ TEM. *Nano Letters* **2014**, *14*, 1745–1750.

22. others,, *et al.* The GMRM Method. *TBD* **2017**, *TBD*, TBD.

23. Batson, P.; Dellby, N.; Krivanek, O. Sub-ångstrom resolution using aberration corrected electron optics. *Nature* **2002**, *418*, 617–620.

24. Dempster, A.; Laird, N.; Rubin, D. Maximum Likelihood from Incomplete Data via the EM Algorithm. *Journal of the Royal Statistical Society. Series B (Methodological)* **1977**, *39*, 1–38.

25. Meng, X.-L.; Rubin, D. B. Maximum likelihood estimation via the ECM algorithm: A general framework. *Biometrika* **1993**, *80*, 267–278.

Graphical TOC Entry